

REPORT DOCUMENTATION PAGE				Form Approved OMB No. 0704-0188	
Public reporting burden for this collection of information is estimated to average 1 hour per response, including the time for reviewing instructions, searching existing data sources, gathering and maintaining the data needed, and completing and reviewing this collection of information. Send comments regarding this burden estimate or any other aspect of this collection of information, including suggestions for reducing this burden to Department of Defense, Washington Headquarters Services, Directorate for Information Operations and Reports (0704-0188), 1215 Jefferson Davis Highway, Suite 1204, Arlington, VA 22202-4302. Respondents should be aware that notwithstanding any other provision of law, no person shall be subject to any penalty for failing to comply with a collection of information if it does not display a currently valid OMB control number. <b>PLEASE DO NOT RETURN YOUR FORM TO THE ABOVE ADDRESS.</b>					
1. REPORT DATE (DD-MM-YYYY) 15-03-2011		2. REPORT TYPE Conference Paper		3. DATES COVERED (From - To)	
4. TITLE AND SUBTITLE  Use of Proper Orthogonal Decomposition Towards Time-resolved Image Analysis of Sprays				5a. CONTRACT NUMBER	
				5b. GRANT NUMBER	
				5c. PROGRAM ELEMENT NUMBER	
6. AUTHOR(S) V. Narayanan, M.D.A. Lightfoot, S.A. Schumaker, S.A. Danczyk, B. Eilers				5d. PROJECT NUMBER	
				5f. WORK UNIT NUMBER 50260538	
7. PERFORMING ORGANIZATION NAME(S) AND ADDRESS(ES)  Air Force Research Laboratory (AFMC) AFRL/RZSA 10 E. Saturn Blvd. Edwards AFB CA 93524-7680				8. PERFORMING ORGANIZATION REPORT NUMBER  AFRL-RZ-ED-TP-2011-086	
9. SPONSORING / MONITORING AGENCY NAME(S) AND ADDRESS(ES)  Air Force Research Laboratory (AFMC) AFRL/RZS 5 Pollux Drive Edwards AFB CA 93524-7048				10. SPONSOR/MONITOR'S ACRONYM(S)	
				11. SPONSOR/MONITOR'S NUMBER(S) AFRL-RZ-ED-TP-2011-086	
12. DISTRIBUTION / AVAILABILITY STATEMENT  Approved for public release; distribution unlimited (PA #10981).					
13. SUPPLEMENTARY NOTES For presentation at The Institute for Liquid Atomization and Spray Systems (ILASS)-Americas; Ventura, CA, 16-18 May 2011.					
14. ABSTRACT  High-speed movies of optically dense sprays exiting a Gas-Centered Swirl Coaxial (GCSC) injector are subjected to image analysis to determine spray characteristics. As a test for its efficacy in analysis of high-optical-density sprays, Proper Orthogonal Decomposition (POD) was applied to the image sequence prior to image analysis. Results of spray morphology including spray boundary, widths, angles and boundary oscillation frequencies, are compared with and without the application of POD. The most dominant modal reconstructions (between 2 and 5) of the spray are found to be sufficient to quantitatively describe the spray parameters, while the frequency of movement of the spray boundary is well predicted by the first two modes alone. Despite being computationally intensive, preprocessing of spray images using POD has advantages in – a) reduction of droplet noise in the spray boundaries thereby resulting in a smoother boundary for edge detection, and b) ability to process morphological parameters of ill-behaved sprays.					
15. SUBJECT TERMS					
16. SECURITY CLASSIFICATION OF:			17. LIMITATION OF ABSTRACT	18. NUMBER OF PAGES	19a. NAME OF RESPONSIBLE PERSON
a. REPORT	b. ABSTRACT	c. THIS PAGE			Dr. M.D.A. Lightfoot
Unclassified	Unclassified	Unclassified	SAR	12	19b. TELEPHONE NUMBER (include area code) N/A

## **Use of Proper Orthogonal Decomposition Towards Time-resolved Image Analysis of Sprays**

V. Narayanan<sup>\*1</sup>, M. D. A. Lightfoot<sup>2</sup>, S. A. Schumaker<sup>2</sup>,  
S. A. Danczyk<sup>2</sup> and B. Eilers<sup>1</sup>

<sup>1</sup>School of Mechanical Industrial and Manufacturing Engineering  
Oregon State University  
Corvallis, OR 97331

<sup>2</sup>Aerophysics Branch, Propulsion Directorate  
Air Force Research Laboratory  
Edwards AFB, CA 93524

### **Abstract**

High-speed movies of optically dense sprays exiting a Gas-Centered Swirl Coaxial (GCSC) injector are subjected to image analysis to determine spray characteristics. As a test for its efficacy in analysis of high-optical-density sprays, Proper Orthogonal Decomposition (POD) was applied to the image sequence prior to image analysis. Results of spray morphology including spray boundary, widths, angles and boundary oscillation frequencies, are compared with and without the application of POD. The most dominant modal reconstructions (between 2 and 5) of the spray are found to be sufficient to quantitatively describe the spray parameters, while the frequency of movement of the spray boundary is well predicted by the first two modes alone. Despite being computationally intensive, preprocessing of spray images using POD has advantages in – a) reduction of droplet noise in the spray boundaries thereby resulting in a smoother boundary for edge detection, and b) ability to process morphological parameters of ill-behaved sprays.

---

<sup>\*</sup>Corresponding author, vinod.narayanan@oregonstate.edu

## Introduction

The advent of high speed imaging as well as other diagnostics allowing time-resolved measurements has offered great advantages to those studying sprays. Researchers have used these diagnostics to enhance their understanding of the underlying physical processes involved in atomization and spray evolution [1-4]. Time-resolved data also provides the ability to study the oscillations that exist in many sprays. However, these new diagnostics produce large quantities of data which must be processed, analyzed and interpreted. Analysis of high-speed movie sequences has relied on image processing to extract quantitative information. And, while established techniques, such as segmentation (thresholding) and edge finding, have proven useful in many cases [3], they have limitations, especially, for example, in experimental facilities that produce optical noise (e.g., droplets being deposited on windows). Additionally, it can be impractical or impossible to extract detailed and accurate time-dependent statistics of complex spray-field dynamics using these typical techniques. This paper, then, focuses on applying Proper Orthogonal Decomposition (POD) to high-speed images of sprays with the aim of extracting higher quality information compared to the “typical” image processing techniques using segmentation and edge detection.

Oscillations occur naturally in many types of sprays due to processes like vortex breakdown (e.g., precessing vortex core-PVC) [5, 6] or the general primary atomization (e.g., hydrodynamic instabilities) [7]. These oscillations can be detrimental to the overall system or application [5]. In combustion devices, in particular, oscillations arising from the spraying process can feed combustion instabilities. These instabilities can, at best, degrade performance and increase emissions or, at worst, directly lead to the destruction of the device. Consequently, the measurement and understanding of spray oscillations are critical to the design of stable, high-performance combustion devices. High-speed imaging has been used to study global spray frequencies [1] and localized frequencies in some systems [2, 4]. As the complexity of the spray increases, however, discerning if and where dominant frequencies exist becomes increasingly difficult. Complex sprays often include multiple frequencies and/or a mixture of periodic and chaotic motions which further complicates data interpretation.

Another complication to data interpretation is that many sprays exhibit high optical densities. These optical densities not only prevent the use of laser diagnostics but can also eliminate the ability to track individual features of the spray (such as surface waves, droplets or clusters of droplets). When individual features cannot be consistently identified in the spray, the processing techniques must rely on global

measurements. This shortfall further complicates the extraction of frequency information; indeed, most investigations of spray oscillation rely on tracking individual features [2, 4, 8]. The high optical densities can also generate a large amount of noise in the images and further reduce the amount of quality of available data.

The POD technique has been applied fairly extensively over the past 15 years in a variety of fields, for example fluid flow [9-11], combustion [12], heat transfer [13, 14] and climatic data [15], to extract the most energetic modes of variability in the data being analyzed. A reconstruction of data using the most energetic modes enables extraction of repetitive patterns that often cannot be discerned by regular image processing. Another advantage of POD is that it permits removal of white noise in the data such as that which would be introduced during image acquisition (e.g., [13]). In relation to POD being applied to spray reconstructions, only a recent experimental paper [16], on liquid jet breakup in cross flow exists. In this study, the authors use POD to reconstruct the jet breakdown at different flow conditions and extract, using spectral analysis, the frequencies and wavelengths of importance. Here, however, the main focus was on specific, localized structures in the spray. With the high-density spray examined here these coherent structures are difficult or impossible to ascertain from the video. There is a lack of literature on the use of POD for high-density sprays, and no comparison with traditional techniques was attempted in the earlier works.

Specifically, in the present work, POD is applied to high-speed video sequences of high-flow rate sprays. The reconstructed spray images (from the POD) as well as raw spray images are processed using identical edge-detection techniques to determine spray features, and results from both methods are compared. The considered dataset consists of backlit images of a specific type of prefilming atomizer, a Gas-Centered Swirl Coaxial (GCSC) injector, whose typical application is rocket engines. Several momentum flux ratios (MFRs), all of which result in high-optical-density sprays, are analyzed. The momentum flux ratio is defined as

$$MFR = \left( \frac{\rho_l}{\rho_g} \right) \left( \frac{\dot{m}_g}{\dot{m}_l} \right)^2 \left\{ \frac{\tau(2r_o - \tau)}{[r_o - (\tau + s)/2]^2} \right\}^2 \quad (1)$$

where  $\rho$  is the density,  $\dot{m}$  is the mass flow rate,  $g$  denotes gas,  $l$  denotes liquid density, and the other, geometric parameters are given in Table 1 and Fig. 1 [17].

## Experimental Methods

The atomizer under study is a specific type of airblast atomizer of interest in rocket engines. Termed a Gas-Centered, Swirl Coaxial (GCSC) injector, the device uses a high-speed central gas core to atomize swirling, annular liquid film. Figure 1 shows a schematic of the injector. Liquid enters four tangentially drilled holes and is initially sheltered from the gas allowing an annular film to develop. Unswirled gas enters along the center of the injector; the gas post contracts very slightly prior to the gas contacting the liquid. While this injector is modular and allows several geometries to be considered, the results presented herein are limited to a single geometry as given in Table 1. The liquid and gas are in contact for 35.2 mm prior to exiting the injector; in all except the minimum momentum flux ratio tested, primary atomization is completed prior to the mixture exiting the injector. More details on the performance of this injector can be found in [17]. Figure 1 and subsequent figures show the flow as moving from left to right; however, the tests are conducted with flow moving in the direction of gravity.

In all of the conditions tested, the GCSC injector produces an optically dense spray. The optical density and other key parameters were a function of the operating conditions, the MFR in particular. In the current set of experiments, the MFR was varied from 48 to 763 as shown in Table 2. The lowest momentum flux ratio, 48, is not discussed here because the atomization did not occur completely within the injector cup and the resulting spray is, therefore, different in character. Table 2 also gives the mass flow rates provided to achieve these momentum flux ratios. The mass flow rates were metered using a cavitating venturi (liquid) and a sonic nozzle (gas). Both metering devices were calibrated using catch-and-weigh techniques. Pressure upstream of the metering devices was recorded and related to mass flow rate while downstream pressures were monitored to ensure that the venturi was cavitating and that the nozzle was choked. A valve was used downstream of the cavitating venturi to limit the pressure drop across the venturi: the targeted pressure drop was between 20 and 50 percent of the total pressure drop. Pressure transducers were calibrated prior to testing using a calibrated pressure source. The accuracies of the transducers and calibrations produce mass flow rates which are accurate to 0.227 g/s. In all cases, the spray exits to atmospheric conditions; because these experiments were conducted above sea level, typical atmospheric pressures are in the range of 91.0 kPa to 93.7 kPa.

Video images were captured using a Vision Research Phantom v7.3 high-speed camera. The camera captured images with a 14-bit pixel depth (i.e., intensity level). The analyzed video was recorded at 6688 frames

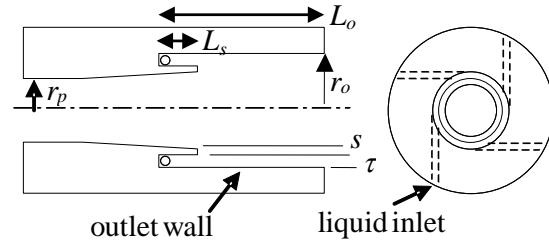


**Figure 1.** A schematic of the GCSC injector is shown. The gas flow would be from left to right while the liquid enters through the tangential holes of radius  $r_{inlet}$ .

t	1.65
s	1.52
$r_o$	7.62
$r_p$	6.35
$r_{inlet}$	1.535
$L_s$	3.2
$L_o$	35.2

**Table 1.** The injector dimensions are given in mm.

Test Label	$m_l$ (kg/s)	$m_g$ (kg/s)	MFR	FOV (H x V) (pixels)
50	0.0579	0.0227	48	377 x 381
200	0.0441	0.0349	199	410 x 461
350	0.0448	0.0449	320	339 x 460
500	0.0369	0.0454	478	338 x 452
650	0.0484	0.0685	633	358 x 456
800	0.0441	0.0685	763	504 x 337

**Table 2.** In addition to flow conditions and the field of view, the test labels used in the text are given.

per second with shutter speeds from 5-30 microseconds. The exposure time was kept fixed at 5  $\mu$ s for all recorded movies. All video is taken with a resolution of 8.9 pixels/mm.

The back lighting was provided by a 500-Watt halogen floodlight. A diffuser was used to provide more uniform lighting; however, nonuniformities in intensity did remain in the background. As a result, a background image was taken at the beginning of each testing day and was subtracted from the spray images as part of the processing procedure described in the Data Analysis Methods section.

## Data Analysis Methods

### Image Preparation

All image processing was performed using Matlab (2008b). Each movie file was in a binary file format proprietary to Vision Research (.cin format) and consisted of 10,154 images. The cin-format file was first converted to 10,154 separate ASCII files. Since the

subsequent image processing with POD was computationally intensive, the field of view and number of frames analyzed were reduced. The time series was downsampled to, typically, 1500 images for POD and 3000 images for raw data analysis, while holding the framing rate fixed at 6688 frames per second. A reduced field of view (FOV) was chosen custom to each test condition (see Table 1) such that this FOV included the most important regions of the spray, vis., the region near the injector, while eliminating the maximum amount of the injector and sprayless background. In order to account for spatial variations in background lighting, the image with no spray (background) was subtracted from each spray image. These background images were taken prior to testing every day.

#### POD preprocessing

As mentioned earlier, the background-subtracted, reduced FOV images were processed using POD prior to image analysis using edge detection. Identical images were also subjected to edge detection without undergoing POD preprocessing and the results compared as a test for POD in spray analysis. Owing to computational memory limitations, only between 1300 and 1500 background-subtracted, reduced-FOV images from the time sequence were used in the POD analysis. The intensity value at each pixel in each background-subtracted, reduced-FOV image in the movie sequence was converted to a single row vector of spatial locations; the series of such row vectors at consecutive time intervals were assembled to form a large  $Z_{n \times m}$  matrix with dimensions corresponding to  $n$  times and  $m$  spatial locations,

$$Z_{nm} = \begin{bmatrix} z_{11} & z_{12} & \dots & z_{1m} \\ z_{21} & z_{22} & \dots & z_{2m} \\ \vdots & \vdots & \ddots & \vdots \\ z_{n1} & z_{n2} & \dots & z_{nm} \end{bmatrix} \quad (2)$$

In the present study, the number of pixel locations exceeded the time instances by an order of magnitude. As outlined in [18], a singular value decomposition has computational advantages when one dimension of a matrix is much larger than the other. Hence, a singular value decomposition was performed on this matrix to yield three matrices,  $U$ ,  $S$  and  $V$ ,

$$Z_{nm} = U_{nn} S_{nn} V_{nm}^t \quad (3)$$

The matrix  $U$  consisted of the normalized expansion (amplitude-time) coefficients, the diagonal matrix  $S$  consisted of the square-root of the eigenvalues, and the matrix  $V$  consisted of the eigenvectors of the decomposition. Eigenvectors are uncorrelated in space

and expansion coefficients are uncorrelated in time. The original data was reconstructed as

$$z_{nm} = \sum_{k=1}^{N_{modes}} a_{nk} F_{km} \quad (3)$$

where  $a_{nk}$  constitute the elements of the expansion coefficient matrix, a projection of the original data onto each eigenvector. Alternately, expansion coefficients can be evaluated by multiplying  $U$  with  $S$ .

After performing a POD, the spray data was typically reconstructed using the first, i.e., most energetic, 2 modes, the first 5 modes and the first 8 modes. For the lowest momentum-flux-ratio (test 50), up to 50 modes were reconstructed. Typically, in between 93 (for test 50) and 99 (for test 800) percent of the spray intensity was described by the very first mode, which constituted the time-mean intensity of the spray. Figure 2 shows a plot of the eigenvalues for different modes, beginning from mode 2, for all MFRs tested indicating an exponential decrease in spray intensity that is attributed to the higher modes.

While the eigenvalue plot in Fig. 2 suggests that higher-order modes are irrelevant, it is important to understand what these modes represent. Typically, higher-order modes in POD reconstructions have been attributed to experimental noise (for example, [13]). Figure 3 shows a reconstruction with various modes of a snapshot for the 200 experimental condition. Note that each image is normalized with the maximum intensity within that image, thereby permitting a qualitative comparison of intensities between images. Figure 3a shows the raw image and Figs. 3b-3d represent reconstructions of this image using modes 1,

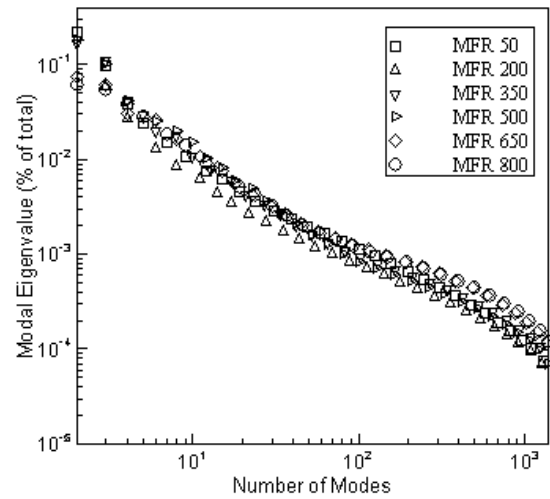


**Figure 2.** The modal eigenvalues for the different MFRs indicate the modal contributions to spray intensity. The Mode 1 eigenvalue is not plotted.

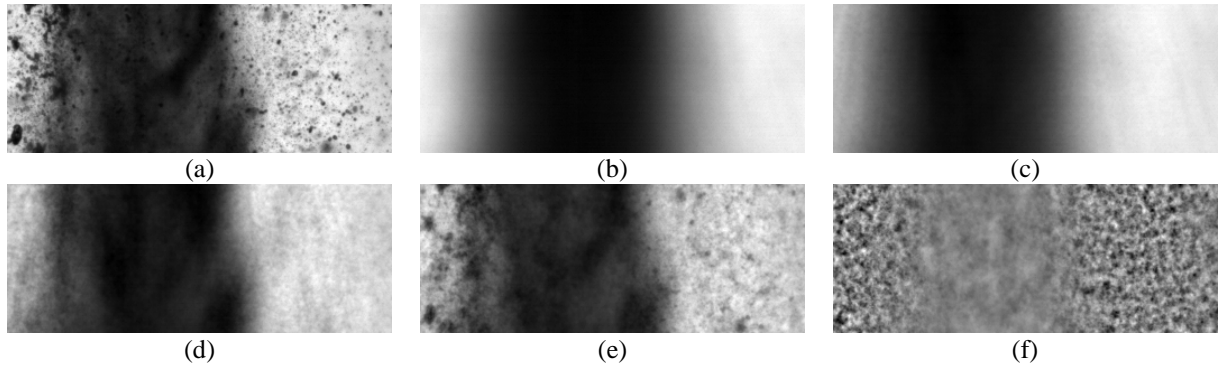


**Figure 3.** These images compare the raw data with the POD modal reconstructions for a highly cropped FOV at the 200 test condition. Compared here are (a) raw data, (b) mode 1, (c) modes 1-5, (d) modes 1-30, (e) modes 1-300, and (f) modes 300-400. Here flow is from the top to the bottom of the image.

1 to 5, and 1 to 30, respectively. While the first mode reconstruction captures the general area of the spray, no transient variations are captured. The reconstruction using the first 30 modes begins to capture intensity variations within the core of the jet, but does not capture droplets on the spray boundary. Figure 3e shows a reconstruction using the first 300 modes. It is seen that a reconstruction on the order of 300 or so modes is needed in order to truly capture the spray details such as larger droplets near the boundaries. Smaller droplets that are not a part of the main spray are still not captured in this reconstruction. Figure 3f shows reconstructions based on modes 300 to 400 and indicates that most of the intensity that is captured by these higher modes are outside the main spray boundary. The intensity variations captured are a combination of both smaller droplets as well as imaging noise. Hence, it can be concluded that whereas higher order modes do not represent noise in a spray reconstruction, the main morphological characteristics of the spray (such as boundaries, widths and angles) as well as the global spray frequencies can be captured by reconstructing only the most energetic modes (less than 5). What is lost when reconstructing only a handful of modes here is the slow-moving droplets in the outer flow field.

#### Edge Detection

The edge detection process uses image segmentation to determine which parts of the image are spray and which are background. First, the image preparation steps and background subtraction, as outlined above, are performed. Two different types of segmentation were considered here. The first used Otsu's method to determine the threshold for segmentation. The implementation of Otsu's method built-in to Matlab's 2008b version was used [19, 20]. The second segmentation was a straight-forward k-means clustering approach where the pixels are clustered into fore- and back-ground clusters. Pixels

were iteratively placed into the cluster whose center was nearest their value and then a new cluster center was determined from the average of the pixels within it. Once no pixels change clusters, the method has converged and the average between the two cluster centers is the intensity level used for segmentation. The k-means clustering approach can be sensitive to the initial cluster choices. Here, the four corners of the image from 10 pixels downstream of the injector outlet to the end of the frame were used for the initial background value (they tend to be some of the brightest pixels) while the remaining pixels from the injector outlet to the end of the frame were used for the initial foreground cluster center. Because the spray and the background are not steady, the threshold values determined from the segregation methods are not identical across the frames of a single-test-condition video. As a result, the instantaneous values, i.e. the values determined for a specific frame, were not the only values considered. Two additional threshold values were determined from the average value of each method over the range of frames examined. Therefore, a total of four different threshold levels were considered for each frame of video. The difference between these four methods was small both in threshold level and in the resulting detected edge.

Once the threshold value was determined, it was used to produce a black and white (binarized) image. The Matlab function `bwboundaries` was then employed to find the outline of the spray [20]. An 8-connected neighborhood with Matlab's "no holes" setting was used. Only the main body of the spray was considered, any traced areas prior to the injector outlet or of isolated droplets or droplet groups were discarded. An example black and white image from which the boundary is determined is given as Fig. 4a. A typical raw image with the resultant traced boundary overlaid is given as Fig. 4b for comparison. Figure 4c overlays the boundary found in the two mode reconstruction from the POD pre-processed data. Figure 4d shows the

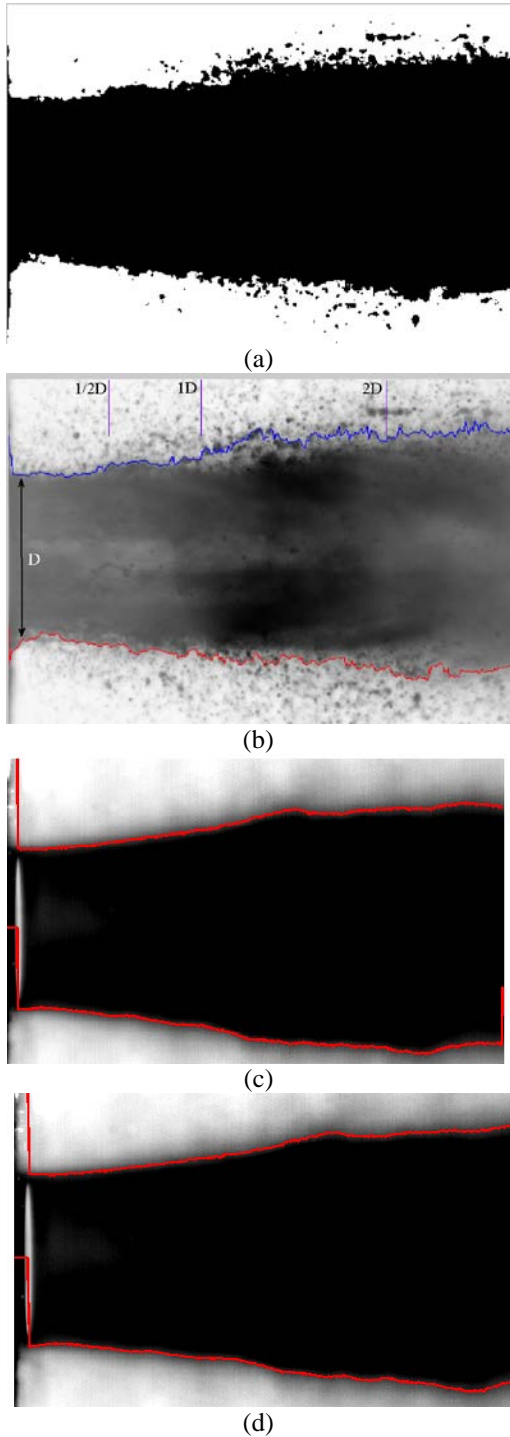


**Figure 4.** The black and white image (a) determined from using the instantaneous Otsu's method on the raw image is compared with the raw image where the boundary, found using this method, has been overlaid (b). These raw image and its found boundaries are less smooth than the image and boundaries determined, using Otsu's method, from the POD-preprocessed reconstruction of 2 modes (c) and 5 modes (d).

boundary detected for the 5 mode reconstruction of the POD pre-processed image. The flow condition shown in Fig. 4 corresponds to the highest momentum flux ratio, test 800.

Once the boundary of the spray was determined, it was used to find various parameters of importance. The spray width was determined by calculating the distance between the two boundaries. This width was halved and added to one boundary of the spray to determine the centerline. Both the width and the centerline were calculated at each pixel in the downstream direction from the injector outlet to the end of the FOV.

Spray half-angles were determined from fitting a line to the spray boundaries; a  $0^\circ$  angle would result if the spray exited with no expansion while a  $90^\circ$  angle would result if the spray expanded to the point it wetted the wall comprising the injector outlet (see Fig. 5). The angle was determined by pinning a line at the injector exit at a location determined by averaging the fifth through ninth (downstream) boundary pixels. The fifth through ninth pixel was used in order to avoid aliasing of the spray exit location by droplets on the injector surface. Because the spray angle is not constant in the downstream direction and because there is noise in the data, angles were determined along several downstream distances. These distances were based on the initial diameter ( $D$ ) of the spray, which, again, was determined by averaging the value at the fifth through ninth downstream locations. Angles were calculated for distances of  $1/2D$ ,  $1D$ , and  $2D$ . Spray angles were determined for each side of the spray and for the centerline as a function of distance.

Fast Fourier transforms were used to examine the spectral content of these results. Specifically, the spectral content of the spray angles, the width, centerline and boundary location were considered. The transforms of the width, centerline and boundary were calculated at the same distances over which angles were determined— $1/2D$ ,  $1D$ , and  $2D$ .

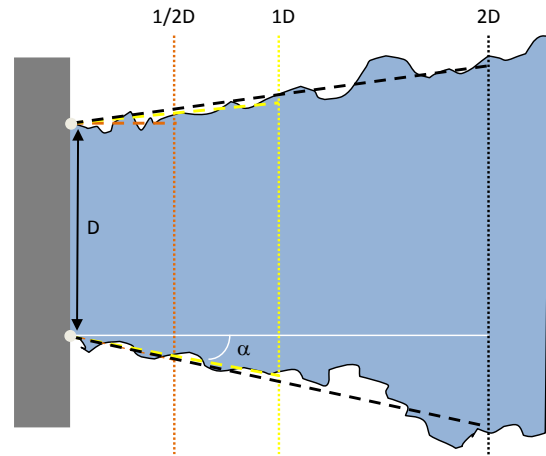


**Figure 5.** This cartoon illustrates the method of determination of angles at various normalized downstream distances,  $L/D$ .

## Results and Discussion

### Comparison Between Segregation Methods

The different segregation methods—Otsu's method and k-means clustering—resulted in different threshold values. Matlab defines the threshold values in terms of percentage of the full-scale intensity value—the images examined here are 14-bit images. Instantaneous threshold value ranged from 68.6 to 79.1 percent. For a specific momentum-flux-ratio condition and boundary (as each half of the image is examined separately), the variation of threshold level is between 4.1 and 7.7 percentage with the average of the raw (not POD preprocessed) videos being 5.7 percent. The variation across time is essentially identical for both segregation methods. The threshold values averaged across frames at each condition differ by 0.2 percent in all cases, with Otsu's method giving the lower value. The averaged thresholding values range from 70.8 to 75.1 percent. As would be expected from such low variability between methods, the different methods had very little impact on the extracted data. For example, a change in the segregation method changed the found boundary location of the raw images by less than 2 pixels on average. Deviations of the boundary from one method to the next tended to be at a single point or over a very small distance ( $<10$  pixels) and were generally under 10 pixels, but some isolated points have single-frame deviations over 50 pixels. Again, the video resolution was 8.9 pixels per mm. There were no systematic deviations or shifts in the boundary location found in the comparison of the methods. The 200 test had the largest single and average deviations. This test was most sensitive to changes in part due to the scattered light by pendant droplets on the injector face and the large droplets on the periphery of the spray. These latter droplets were seen only when POD was not employed or when large numbers of modes were reconstructed. Figure 6 illustrates the typical variation in boundaries determined by the four different segregation methods for the 200 test condition at the first recorded frame and at a frame with one of the largest deviation, frame 2745 ( $t=0.4104$  s). The results shown in Figure 6 are for images not preprocessed using POD; the variation in the POD-processed results is lower. As a result of the low variability, only the results using Otsu's method as determined for each individual image (i.e., instantaneous, not averaged) are reported in the following sections.

### Comparison Between POD Preprocessed and Raw Data Results

The raw data as well as the POD-preprocessed data were subjected to the above-described segregation methods to determine the spray boundaries. Reconstructions of the first 2 modes, the first 5 modes

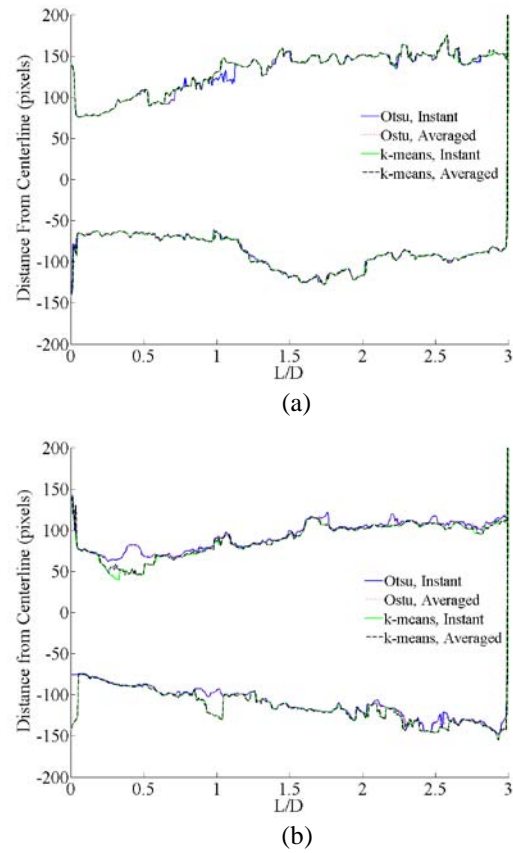


**Figure 6.** The found boundaries for the four different segregation techniques are shown for the case with the worst agreement, 200. Both a typical image (a) and one of the worst images (b) are shown.

and the first 8 modes are performed for MFRs between 200 and 800. To compare the results, several measures are quantified including the instantaneous spray widths, the spatially-averaged variability with time of the boundaries, time-variation of boundaries, and the corresponding frequency variations of boundaries at these locations. Spray angles at  $L/D$  of 0.5, 1 and 2 are also considered.

Figures 7a and 7b shows a comparison of the instantaneous spray widths, for a particular image in the movie sequence, between the POD-preprocessed data and the raw data for the tests labeled 200 and 800, respectively. For both cases, the spray width increases at a greater rate in the regions near the injector face ( $L/D < 2$ ) and the growth rate remains somewhat stagnant following this  $L/D$  location. Also, as is to be expected based on the inertia of the gas core, the spread of the higher MFR condition (800) spray is smaller than that of the lower MFR condition (200) spray. As can be seen for both MFR sprays, the raw data and POD data agree fairly well, with the widths from the POD preprocessed data showing little difference between the



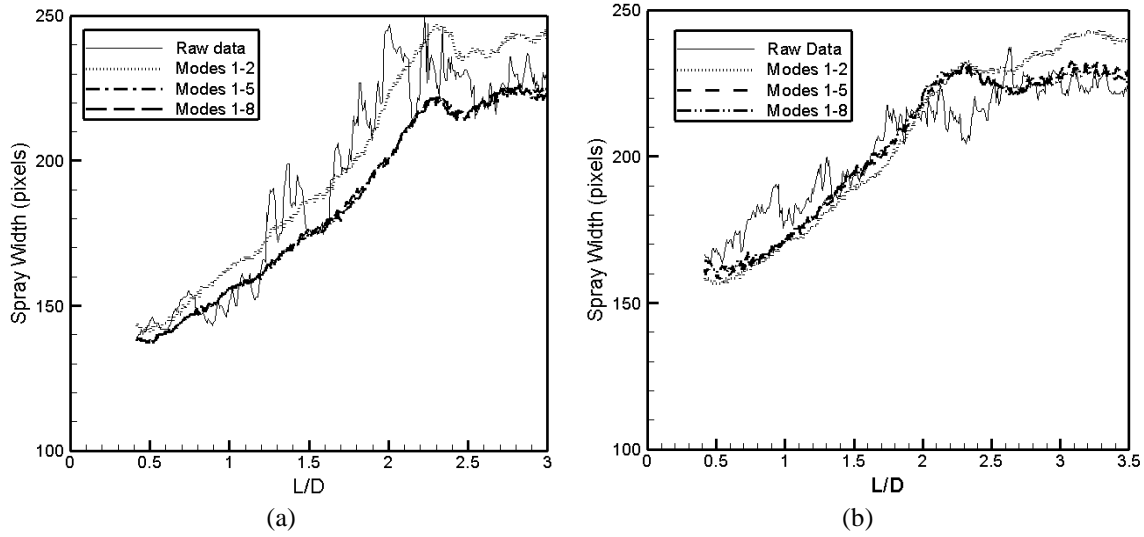


**Figure 7.** Comparison of spray width between raw and POD preprocessed images are shown for condition (a) 200 and (b) 800

5 mode and the 8 mode reconstructions. The spray widths in the raw data show large variations with downstream distance,  $L/D$ , potentially due to the inclusion of droplets at the spray edges (see for example, Figs. 3a and 6). Reconstructions using POD, as seen in Fig. 3, tend to filter these droplets resulting in a much more uniform spray boundary that can be easily detected. The differences between the POD-preprocessed data and the raw data are reduced for the 200 test compared to the 800 test, as is to be expected, since the boundary is better defined for the 800 spray.

Figure 8 shows typical time series of the bottom spray boundary location at a downstream distance  $L/D$  of 1.0 for the 200 spray. The three POD-preprocessed trends are shown in this figure along with the trend from the raw (not preprocessed) results. Both raw and POD-preprocessed data show identical trends with time in terms of periodicity of boundary movement. The POD-preprocessed boundary variations are less noisy in general, and this highlights the use of POD as a filtering tool for spray analysis. As will be seen in the spectral analysis, dominant frequencies are more readily identified using a POD-preprocessed time series. Overall, a substantial amount of variation in time was seen in the location of the boundaries, width and centerline over time for both raw and POD-preprocessed data. In some tests, most notably 200, a large portion of the temporal variation is seen to be periodic; in other tests, the variation appears random or perhaps at too high a frequency to discern with the naked eye. As the measurement location moved downstream, more variation was seen in the boundary, width and centerline positions. The width had the most time variations while the centerline had the least; the variation in the two boundaries was essentially

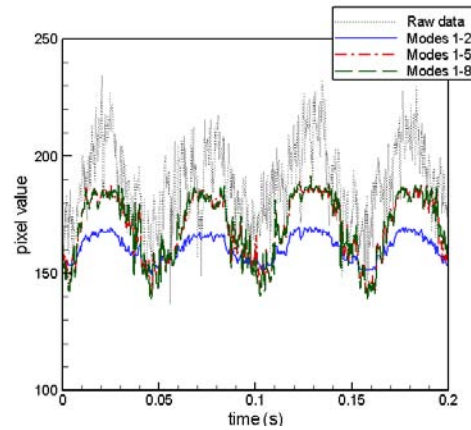


**Figure 8.** A comparison of the location of the spray boundary at  $L/D=1.0$  as a function of time between the POD-preprocessed and raw data is shown.

identical. Throughout, however, the variations in the POD preprocessed results were smaller than those in the raw results.

Table 3 provides the standard deviation of the top and bottom spray boundaries as determined by the spatial average of the temporal standard deviation. This standard deviation value is chosen to represent the global variability of the spray boundary with time. In general, the POD-preprocessed data have less deviation for all examined reconstructed modes when the MFR is equal or above that of case 500. For the 200 case, the POD-preprocessed data have less deviation with 2 modes reconstructed, nearly equal variability when 5 modes are reconstructed and show about a 10% increase in variability for the reconstructions of modes compared with variability measured from the raw data. This result likely stems from the fact that much of the

	Raw Data (pixels)		POD Data (pixels)		
MFR	Boundary1	Boundary2	Modes	Boundary1	Boundary2
200	17.7	18.3	1-2	11.0	11.2
			1-5	18.6	18.9
			1-8	19.7	19.6
350	8.7	9.9	1-2	5.8	1.4
			1-5	10.2	5.8
			1-8	10.6	7.1
500	8.2	8.8	1-2	3.2	4.0
			1-5	6.9	7.4
			1-8	8.0	8.1
650	5.7	5.9	1-2	2.1	1.1
			1-5	4.1	3.2
			1-8	4.9	3.6
800	5.9	5.6	1-2	1.9	0.4
			1-5	3.7	2.8
			1-8	4.2	3.9

**Table 3.** Spatially-averaged standard deviations of top and bottom spray boundaries are determined from the raw and POD-preprocessed data.

variability in the 200 boundary is from organized, periodic motion. While POD is effective at filtering out errors and noise due to erroneous information such as mistaking large droplets for the boundary, it does not suppress and, indeed, seems to highlight, variability due to organized motion. For the 350 case, the agreement is better for one boundary than the other. This may indicate that one boundary is more unsteady than the other; the POD preprocessing can reduce the noise due to droplets but appears (from case 200) to highlight the variability due to periodic motion. In general, the POD reconstructions with the first two modes under-predicted the spray variations in time, while the reconstructions using the first 5 and 8 modes more closely resembled the raw data predictions. These results as well as the match of the instantaneous boundary widths (Fig. 7) indicate that on the order of 5 or 8 modes of reconstruction is necessary to properly predict the spray boundary variations in space and time.

As would be expected from variations in boundary location, the spray angles vary with time. The level of variation in the spray angles is similar for both boundaries in most cases. Angles fit over a longer distance, e.g. 2D versus 1/2D, have less variation over time. The spray angle decreases as the fit extends over a greater distance (as expected from the width variation shown in Fig. 7); the centerline is essentially constant for most cases but sometimes exhibits a noticeable decrease. Figure 9 compares the time-averaged spray angles with error bars representing their standard deviation across the different processing approaches for the 800 spray. As can be seen, the average values and standard deviations obtained from the raw data processing and POD-preprocessed data show very good agreement at all L/D distances analyzed, further indicating that the POD reconstructions with 5 most

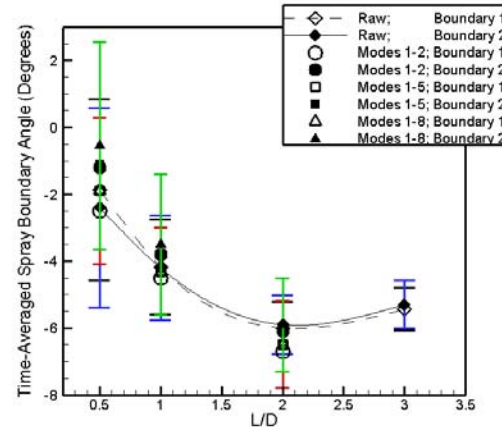


**Figure 9.** Comparison of time-averaged spray angles between raw and POD-preprocessed data for the 800 spray shows good agreement.

dominant modes accurately capture the morphology of the spray.

Whereas the above results indicate the utility of POD as a method for filtering boundary droplets that might cause erratic noise in image processing, POD's real strengths lie in the extraction of energetic modes and, therefore, any global periodic patterns that exist in the spray. Figures 10a-d show a series of frequency plot comparisons between POD-preprocessed data and raw data. Figures 10a and 10b show the power spectrum of the top boundary variation in time for condition 200 at an L/D of 0.5 and 1.0, respectively. Figures 10c and 10d show the same for condition 800. As can be seen from Fig. 10a and 10b, the lower MFR condition spray had a clear periodic behavior with a frequency of ~ 20 Hz. The raw data as well as the POD-preprocessed data clearly indicate this peak at both L/D locations. In addition, it can be seen that the energy content at other

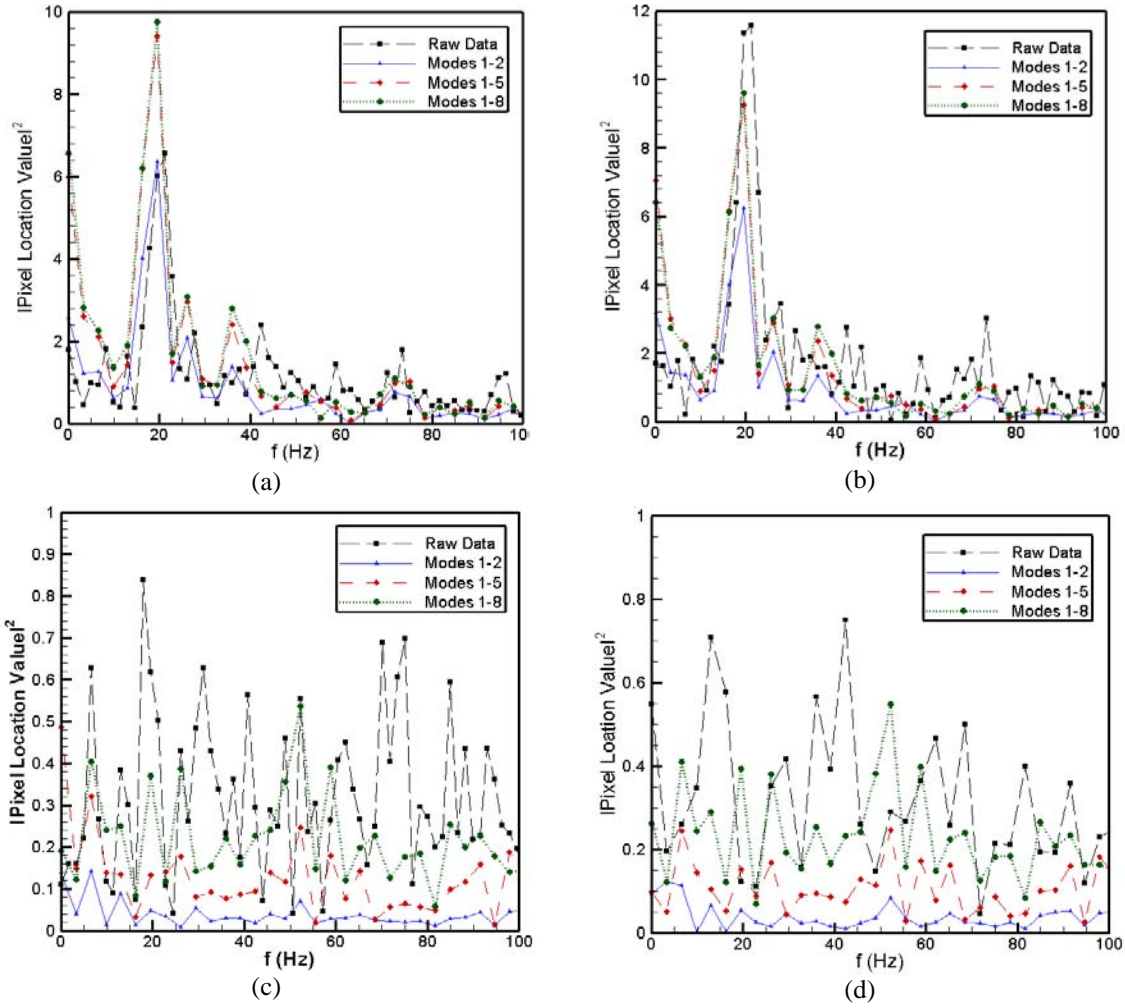


**Figure 10.** The power spectra of top boundary variations versus time allow a comparison of the preprocessing techniques for the images from (a) case 200,  $L/D = 0.5$ ; (b) case 200,  $L/D = 1.0$ ; (c) case 800,  $L/D = 0.5$ ; (d) case 800,  $L/D = 1.0$ .

frequencies are generally lower, compared to the peak frequency energy content, for the POD-processed data than for the raw data, thereby making it easier to distinguish dominant frequencies. As a measure of the difference in energy content between the dominant frequency and the next highest peak (typically noise), a dominance factor is defined as

$$D(\%) = \left( \frac{|pixel\ value|_{dominant\ peak}^2}{|pixel\ value|_{second\ peak}^2} - 1 \right) \times 100 \quad (5)$$

For the 200 case at 0.5 and 1.0  $L/D$  the dominance for the raw data is 21 percent while it is 219 percent and 223 percent for the POD-preprocessed data with 8 modes reconstructed. The raw data has a secondary peak at 19.5 Hz which is not as strong in the POD-preprocessed data. The dominance between the secondary 19.5 Hz peak and the third-highest peak in

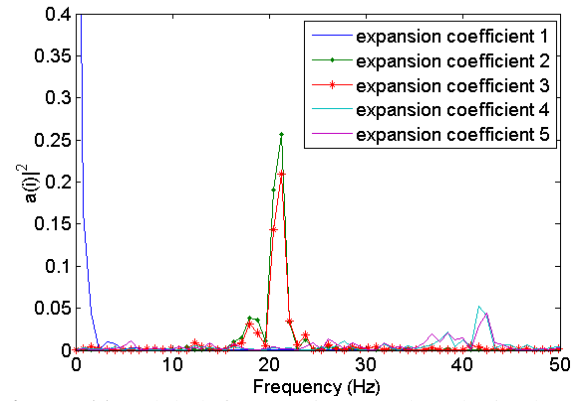


**Figure 11.** Global frequencies can be obtained as shown in Eq 6. Here, the first 5 expansion coefficients are given.

the raw data is nearly equal to the dominance of the two highest peaks for the 8-mode reconstructed data. Figure 10c and 10d show the spectral analysis results for the 800 spray. No clear peak can be identified using the raw data or the POD reconstructions. While the raw data and 8 mode reconstructions show several peaks, a look at spectra of modes 2 and 5 clearly indicates that there is no clear dominant frequency in the boundary variation with time at either location. Global frequencies can also be extracted from POD without the need for processing it through the edge detection program. The dominant expansion coefficients, which are obtained by a projection of the data matrix  $Z$  onto the eigenvectors,

$$\vec{a} = Z\vec{f}_t \quad (6)$$

also showed a dominant peak around 20 Hz for the 200 spray, as seen in Fig. 11. Note that the first expansion coefficient represents the projection of the mean and hence does not show any spectral content, while the second and third expansion coefficients show the 20 Hz peak.

## Conclusions

The use of proper orthogonal decomposition as a preprocessing tool to image analysis of high-optical-density sprays is presented. Comparisons are provided of spray morphological parameters using POD preprocessed images as well as raw images. In general, good agreement is found to exist between the results of spray parameters using both methods. POD preprocessing is shown to help with reduction of spatial variations in the spray boundaries due to the presence of edge droplets. POD allows two different methods for determining dominant frequencies. Using the same spectral analysis methods for both preprocessed and raw sprays shows that the dominant frequencies are more readily identified in the POD preprocessed results.

## Acknowledgements

Vinod Narayanan and Benn Eilers would like to thank the ASEE Air Force Summer Faculty Fellowship program for financial assistance

## References

1. Lightfoot, M.D.A. and Danczyk, S.A., Eleventh Triennial International Annual Conference on Liquid Atomization and Spray Systems, Vail, CO, July 2009.
2. Park, J., K. Y. Huh, X. Li, M. Renksizbulut, *Physics of Fluids* 16(3):625-632 (2004).
3. Pastor, J.V., Arregle, J. and Palmares, A., *Applied Optics* 40(17):2876-2885 (2001).

4. Wang, Q., Mondragon, U.M., Brown, C.T. and McDonnell, V.G., *ILASS Americas, Twenty-second Annual Conference on Liquid Atomization and Spray Systems*, Cincinnati, OH, May 2010.
5. Syred, N., *Progress in Energy and Combustion Science* 32:93-161 (2006).
6. Lopez-Pages, E., C. Dopazo, N. Fueyo, *Journal of Fluid Mechanics*, 515:1-31 (2004).
7. Lefebvre, A. H. *Atomization and Sprays*. New York, Hemisphere Press, 1989.
8. Carvalho, I. S., M. V. Heitor, D. Santos, *International Journal of Multiphase Flow*, 28(5):773-789 (2002).
9. Holmes, P., Lumley, J., and Berkooz, G. *Turbulence, Coherent Structures, Dynamical Systems, and Symmetry*, Cambridge University Press, 1996.
10. Rambo, J., and Joshi, Y., *International Journal of Heat and Mass Transfer*, 50:539-551 (2007).
11. Morse, D., and Liburdy, J. A., 2009, *Journal of Fluids Engineering*, 131:1-12, (2007) paper 051202.
12. Stohr, M., and Meier, W., *Proceedings of the 12<sup>th</sup> International Symposium on Flow Visualization*, DLR, Gottingen, Germany, 2006.
13. Narayanan, V., and Patil, V. A., *Experimental Thermal and Fluid Science Journal*, 32:682-695 (2007).
14. Krebs, D., Narayanan, V., Liburdy, J. A., and Pence, D. V. *Experimental Thermal and Fluid Science*, 34(4):434-445 (2010).
15. Bjornsson, H., and Venegas, S. A., *A manual for EOF and SVD analyses of climatic data*, Center for Climate and Global Change Research Report 97-1, 1997.
16. Arienti, M., and Soteriou, M. C., *Physics of Fluids*, 21:1-15, (2009), paper no 112104.
17. Schumaker, S.A., Danczyk, S.A. and Lightfoot, M.D.A., *48th AIAA Aerospace Sciences Meeting*, Orlando, Florida, January 2010, AIAA 2010-368.
18. Chatterjee, A., *Current Science*, 78:808-817 (2000).
19. Otsu, N., *IEEE Transactions on Systems, Man, and Cybernetics* 9(1):62-66 (1979).
20. Matlab R2008b, *Image Processing Toolbox*, MathWorks Inc., Natick, MA, 2008.